Chapter 3:
Single Atom Catalysts Supported on 2D α-SiX (X = N, P, As, Sb, Bi) and Holey Graphyne for HER Activity

3.1 Introduction

Rising energy needs from technology and population growth, coupled with dwindling traditional sources, challenge researchers seeking alternative vehicle propulsion fuels.[1] Combatting these issues demands clean and sustainable energy sources. Hydrogen emerges as a top contender, with renewable reserves and minimal emissions. Its advantages include high energy efficiency, abundant availability, emission-free production from water and superior energy density.[2] The HER activity for water splitting stands as a vital method for hydrogen production, especially with clean energy sources like solar and wind power, bolstered by effective catalysts.[3] Efficient catalysts are pivotal for hydrogen production via water electrolysis. While Pt and Pd are benchmarks, their cost and scarcity limit broad usage.[4] Thus, the race is on to develop cost-effective catalysts, essential for a thriving hydrogen economy.[5]

Single-atom catalysts, abbreviated as SACs, are composed of discrete metal atoms positioned upon a supporting material. They offer remarkable catalytic advantages: single active sites, efficient metal utilization, strong metal-support interactions and exceptional performance.[6] Efforts focus on replacing pure noble metal catalysts with SACs, even anchoring them on non-noble supports, to advance renewable energy technologies.[7] The urgency lies in creating cost-effective, efficient non-noble-metal SACs.[8] To design SACs, numerous studies have explored transition metals decorated to 2D substrates like graphene, h-BN, silicene, graphyne, antimonene, graphdiyne, C_8N_8, C_2N etc., leading to promising results in terms of their HER activity.[9-15] The combined theoretical and experimental study investigates the utilization of transition metals (such as V, Co, Rh, Cr and Fe) anchored on N doped graphene

to fabricate SACs for catalytic activity of HER. The findings demonstrate that Co anchored N doped graphene exhibits the lowest Gibbs free energy of 0.13 eV, indicating its utility for efficient catalytic activity for HER.[9] One of the theoretical studies investigated the catalytic activity for HER by incorporating different transition metals over defected graphene and h-BN structures as SACs. The results highlighted that many of these SACs exhibit HER performance that is close to the ideal value.[10] Sun et al. showed that the pristine 2D silicene is inactive for HER, while transition metals (V, Fe, Ti, Mn, Ni, Co, Cr, Be) anchored silicene exhibits efficient HER activity, with Gibbs free energy values ranging from -0.09 to 0.18 eV.[11] Furthermore, in the domain of DFT investigations, the study explored the construction of SACs using graphyne as a supporting matrix for first-row transition metals. The findings revealed that among these SACs, Ni supported on graphyne exhibited a HER activity performance that closely approached to ideal.[12] In addition, Song et al. investigated the HER activity of defective 2D antimonene by anchoring eighteen distinct transition metals. Among these, it was found that Ir and Pt anchored to defective 2D antimonene as SACs demonstrated commendable catalytic activity for HER, with a Gibbs free energy of -0.01 eV for both.[13] Similarly, using DFT simulations, Tianwei et al. designed transition metals anchored graphdiyne as SACs and found that Pt and Ni anchored graphdiyne SACs exhibit promising results for the full water splitting reaction.[14] Recently, Chen et al. fabricated SACs composed of various transition metals (Mn, Ti, Cr, Co, Fe, Cu, Ni, Ru, Mo, Rh, Ag, Pd, Au, Pt, W) embedded in 2D C_8N_8 and investigated their HER activity. Among these, Rh anchored C_8N_8 SAC exhibited superior catalytic activity for HER compared to the other SACs.[15] Likewise, the HER activity of the 2D C_2N is elevated through the strategic anchoring of various transition metals, yielding notably improved outcomes when contrasted with the pristine scenario.[16]

As mentioned earlier, materials composed of binary compounds based on group IV and V elements, as well as mono-element compounds of group IV, have been extensively

investigated for their potential as SACs in the context of HER activity. In a recent study, conducted by Burak et al., they effectively demonstrated the existence of dynamically stable hexagonal α-SiX (where X = N, P, As, Sb and Bi) monolayers within the realm of group IV and V elements using DFT simulations.[17] After the prediction, the 2D α-SiX structures were investigated for their thermoelectric properties as well as their performance as catalyst for OER and oxygen reduction reaction.[18-20]

In very recent, a new 2D structure, holey graphyne (HGY), advanced allotrope of graphene, has been synthesized via a Castro–Stephens coupling reaction using 1,3,5-tribromo-2,4,6-triethynyl benzene.[21] HGY's geometry showcases uniform pores with six, eight and twenty-four vertex rings surrounded by zero, two and six acetylene linkages (sp-sp bonds).[21] This arrangement connects two carbon atoms of the benzene ring to two carbon atoms of the nearest octagon, yielding sp to sp^2 carbon ratio of 0.50.[21] After the experimental synthesis, HGY has been explored for hydrogen storage, sensing and as an electrode material for batteries.[22-27]

As mentioned above, the α-SiX (where X = N, P, As, Sb and Bi) and HGY monolayers have not yet been studied in the realm of catalysts. In this chapter, we present the design of SACs, which involve transition metals supported on α-SiX and HGY monolayers, utilizing DFT simulations. Additionally, we analysed the structural and electronic properties of both pristine monolayers and monolayers with anchored transition metals. We also investigate their performance in the HER activity. Finally, we validate the superiority of our results by comparing them with previous reports.

3.2 Computational Details

All necessary computational calculations were carried out utilizing first-principles based DFT as implemented in Quantum Espresso code.[28] The exchange-correlation

relationship was handled using Perdew-Burke-Ernzerhof's (PBE) generalized gradient approximation (GGA).[29] To accurately estimate the interaction between absorber and adsorbent, we utilized Grimme's dispersion adjustment (D2) in all calculations.[30] A vacuum of 20 Å was applied in the direction perpendicular to the plane to avoid interaction between two neighboring layers. A kinetic energy cut-off of 70 Ry was adopted for α-SiX monolayers and 50 Ry was adopted for the HGY monolayer, both of which are adequate for achieving convergence in total energy. During structural optimizations, the Brillouin zone (BZ) was sampled using a Monkhorst-Pack k-mesh of 7 × 7 × 1 grid for α-SiX monolayers and 5 × 5 × 1 for the HGY monolayer in reciprocal space.[31] The energy convergence value between two successive steps was set at 10^{-4} eV, and the process was repeated until the maximum Hellmann-Feynman forces acting on each atom were less than 0.001 eV/Å.

3.3 Results and Discussion

3.3.1 Structure and Electronic Properties of Pristine α-SiX (X = N, P, As, Sb and Bi) and HGY Monolayers

3.3.1.1 Pristine α-SiX (X = N, P, As, Sb and Bi) Monolayers

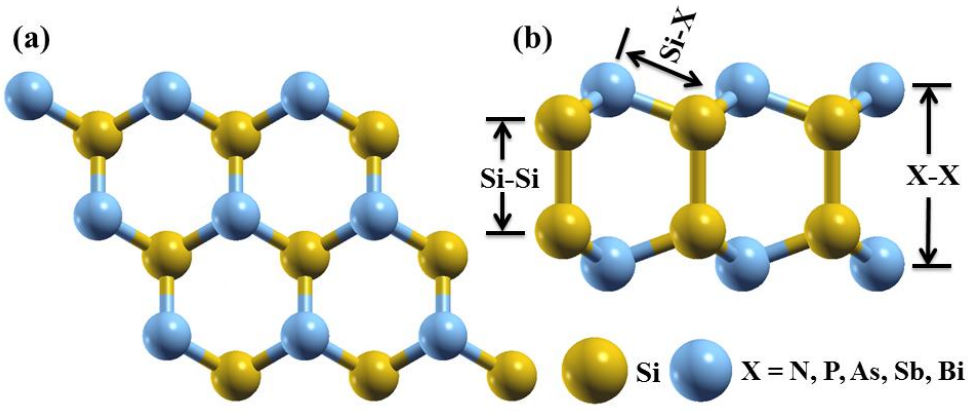

Figure 3.1: Top (a) and side view (b) of α-SiX (X=N, P, As, Sb, Bi) monolayers.

Prior to delving into the exploration of HER activity, the 3×3×1 supercell of α-SiX (X = N, P, As, Sb and Bi) monolayers have optimized. This supercell contained 36 atoms, comprising 18 Si atoms and 18 X atoms. The optimized geometry of the 3×3×1 supercell for

α-SiX monolayers are visually depicted in Fig. 3.1(a and b), illustrating both the top and side views. The resulting structural parameters, encompassing bond lengths and angles, for α-SiX monolayers are presented in Table 3.1. Notably, these calculated parameters exhibit a favourable alignment with earliest reports.[17,18] The lattice parameters are 8.66 Å, 10.54 Å, 11.02 Å, 11.89 Å and 12.16 Å of 3×3×1 supercell of α-SiX (X=N, P, As, Sb, Bi) systems, respectively.

Table 3.1: Structural parameters and band gap of α-SiX (X=N, P, As, Sb, Bi) monolayers, respectively.

Monolayers	Bond length (Å)			Angle (°)		Band gap (eV)	References
	Si-Si	X-X	Si-X	θ_1 (Si-Si-X)	θ_2 (Si-X-Si)		
α-SiN	2.40	3.51	1.75	108.33	110.59	1.75	Present work
	2.43	3.54	1.76	108.40	110.52	1.74	[17]
	2.43	3.54	1.76	108.6	110.56	1.73	[18]
α-SiP	2.35	4.37	2.26	116.56	101.54	1.50	Present work
	2.37	4.41	2.28	116.50	101.62	1.52	[17]
	2.38	4.40	2.28	116.36	101.79	1.49	[18]
α-SiAs	2.33	4.45	2.39	117.61	100.24	1.57	Present work
	2.36	4.57	2.40	117.38	100.54	1.63	[17]
	2.37	4.56	2.39	117.23	100.71	1.64	[18]
α-SiSb	2.32	4.78	2.59	118.60	99.50	1.13	Present work
	2.36	4.82	2.62	117.92	99.85	1.18	[17]
	2.36	4.81	2.62	117.89	99.88	1.19	[18]
α-SiBi	2.31	4.87	2.66	118.66	98.93	0.78	Present work
	2.35	4.92	2.72	118.07	99.66	0.64	[17]
	2.35	4.90	2.72	117.95	99.81	0.67	[18]

The band structure and partial density of states (PDOS) of pristine α-SiX are shown in Fig. 3.2. The α-SiX monolayers (X = N, P, As, Sb) exhibit characteristics of indirect band gap semiconductors with band gaps of 1.75 eV (MK to K), 1.50 eV (KΓ to M), 1.57 eV (Γ to M),

and 1.13 eV (Γ to M), respectively. The α-SiBi is a direct band gap semiconductor with 0.78 eV band gap at the Γ point, consistent with previous DFT studies (refer to Table 3.1).

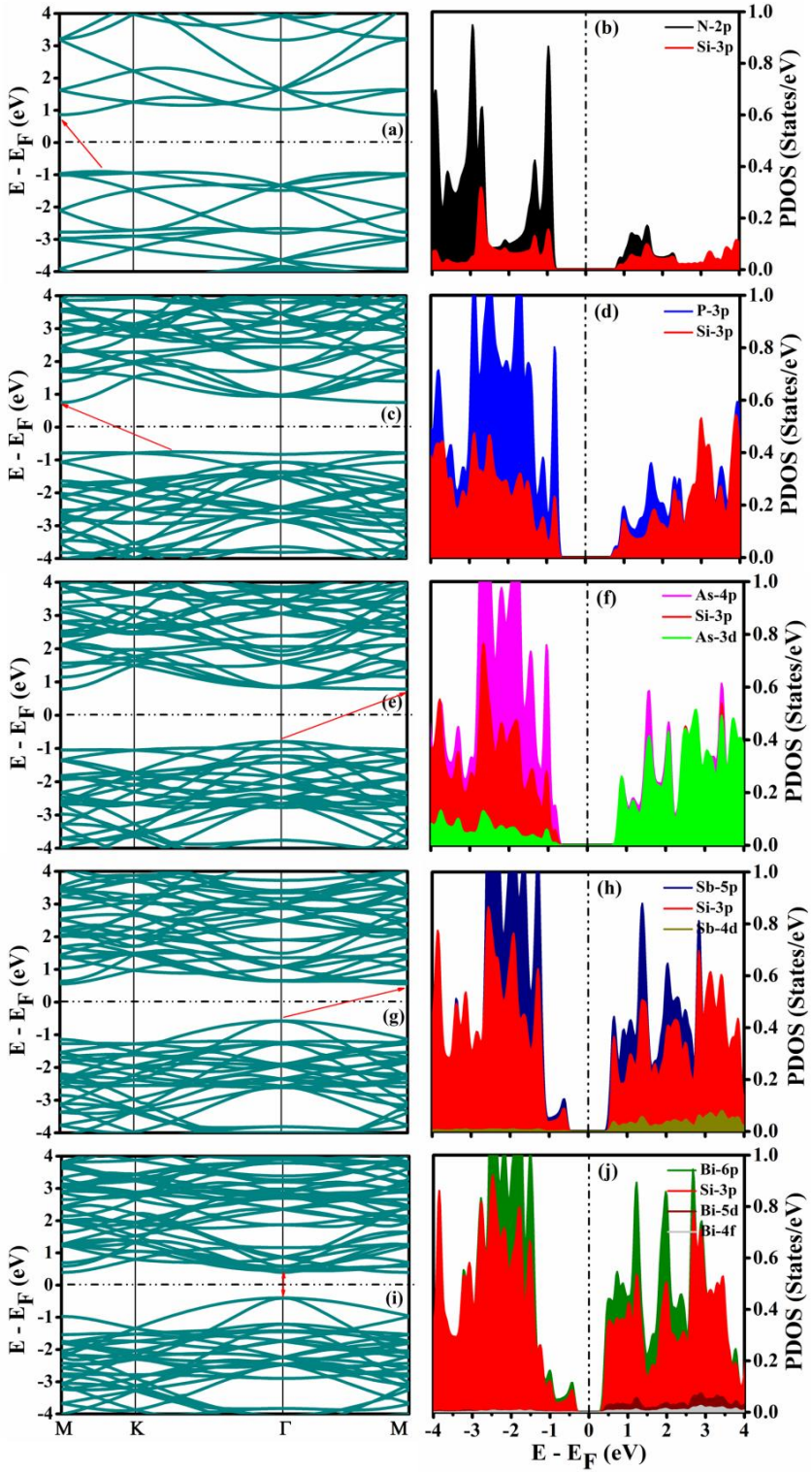

Figure 3.2: Band structure and PDOS of α-SiN (a and b), α-SiP (c and d), α-SiAs (e and f), α-SiSb (g and h) and α-SiBi (i and j) monolayers, respectively.

Analysis of the PDOS of α-SiN and α-SiP (Fig. 3.2(b and d)) reveals that the bonding region (VBM) stems mainly from N-2p orbitals for α-SiN and P-3p orbitals for α-SiP. However, the non-bonding region (CBM) is contributed by N-2p and Si-3p orbitals in α-SiN, and P-3p and Si-3p orbitals in α-SiP. For α-SiX (X = As, Sb, Bi), Si-3p orbitals split evenly between VBM and CBM. In α-SiAs (Fig. 3.2(f)), As-4p orbitals dominate the VBM, while the CBM involves As-4p, Si-3p and As-3d orbitals. In α-SiSb and α-SiBi (Fig. 3.2(h and j)), VBM and CBM arise from balanced Sb-5p and Si-3p orbitals, and Bi-6p and Si-3p orbitals, respectively. Furthermore, α-SiSb demonstrates Sb-4d orbital contributions to the CBM, whereas α-SiBi involves both Bi-5d and Bi-4f orbitals in its CBM. Overall, PDOS analysis highlights orbital overlap and hybridization, emphasizing robust bonding in α-SiX monolayers.

3.3.1.2 Pristine HGY Monolayer

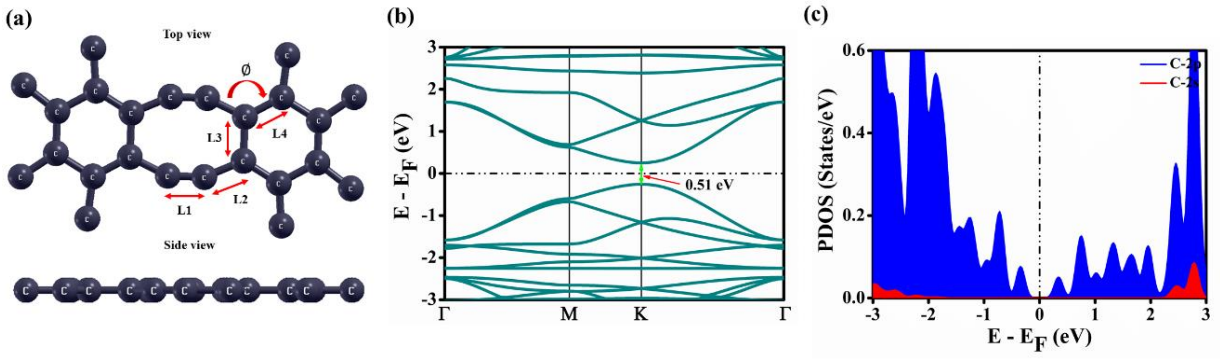

Figure 3.3: Structural geometry (a), band structure (b) and PDOS (c) of HGY monolayer, respectively.

Fig. 3.3(a) shows the optimized structure of the HGY monolayer. The band structure and PDOS are presented in Fig. 3(b and c), respectively. Table 3.2 presents a comparison of the calculated structural parameters (lattice constant, bond lengths as indicated in Fig. 3.3(a) and angle (Ø)) as well as band gap of the HGY monolayer with findings from previous reports. In Fig. 3.3(b), the HGY monolayer demonstrates a direct band gap of 0.51 eV at K point in the BZ. The obtained structural parameters and band gap exhibit strong agreement with the

previous studies.[22-24] The PDOS plot in Fig. 3.3(c) illustrates the division of the C-2p orbital into VBM and CBM, with minimal contribution from C-2s orbitals.

Table 3.2: Comparison of structural parameters and band gap of pristine HGY monolayer with earlier studies.

System	Bond length (Å)	Lattice (Å)	Ø (^{o})	Band gap (eV)	References
HGY	1.22 (L1), 1.45 (L3), 1.40 (L2), 1.39 (L4)	10.79	125.59	0.51	Present work
	1.227 (L1), 1.463 (L3), 1.414 (L2), 1.397 (L4)	10.85	125.80	0.50	[22]
	1.23 (L1), 1.46 (L3), 1.41(L2), 1.40 (L4)	10.85	126.03	0.40	[23]
	1.226 (L1), 1.463 (L3), 1.413 (L2), 1.398 (L4)	---	125.60	0.51	[24]

3.3.2 HER Activity over Pristine α-SiX (X = N, P, As, Sb and Bi) and HGY Monolayers

The estimation of catalytic activity for HER is determined by the change in the Gibbs free energy of the hydrogen (H) atom adsorption (ΔG_H)[32-34]:

$$\Delta G_H = \Delta E^H_{ads} + [\Delta E^{ZPE} - T\Delta S] + G_{pH}$$

$$\Delta G_H = \Delta E^H_{ads} + [\Delta E^{ZPE} - T\Delta S] + [pH \times k_b T \times ln10] \quad \text{-----(3.1)}$$

where ΔE^H_{ads} represents the adsorption energy of H atom over considered system, ΔE^{ZPE} signifies the difference in zero-point energy of the H atom between the adsorbed and gas phases, $T\Delta S$ accounts for the entropy correction term and G_{pH} denotes the pH correction term. From literature, the value of $\Delta E^{ZPE} - T\Delta S$ for H adsorption is 0.24 eV.[32-34] Utilizing this value and considering pH = 0, equation (3.1) takes the following form:

$$\Delta G_H = \Delta E^H_{ads} + 0.24 \quad \text{-----(3.2).}$$

The adsorption energy of the H atom (ΔE_{ads}^{H}) is determined as follows:

$$\Delta E_{ads}^{H} = E(\text{Catlysts} + H) - E(\text{Catlysts}) - E(H_2) \quad \text{-----(3.3)}$$

where E(Catalysts+H), E(Catalysts) and E(H_2) represent the total energy of the system with adsorbed hydrogen, the total energy of the system without hydrogen and the energy of free hydrogen molecule, respectively.[32-34]

To study the catalytic activity of the HER of the bare 2D α-SiX (X = N, P, As, Sb, Bi) systems, we initially positioned H atom above all possible locations. Utilizing equations (3.1, 3.2 and 3.3), we determined the values of ΔE_{ads}^{H} (ΔG_H) to be 0.56 eV (0.80 eV), 0.82 eV (1.06 eV), 1.29 eV (1.53 eV), 1.36 eV (1.60 eV) and 1.18 eV (1.42 eV) for the α-SiX systems, respectively. The significantly positive values of ΔE_{ads}^{H} and ΔG_H indicate that this pristine α-SiX systems are inefficient for catalytic activity for HER. Likewise, in the examination of catalytic activity of HER within the bare HGY sheet, we positioned H atom at various sites. The resulting values for ΔE_{ads}^{H} and ΔG_H were determined as 0.16 eV and 0.40 eV, respectively. Notably, the calculated ΔG_H value significantly deviates from zero, signifying its lack of suitability for catalytic activity of HER similar to bare α-SiX systems.

3.3.3 Binding Energy for Transition Metal Anchored α-SiX (X = N, P, As, Sb and Bi) and HGY Monolayers

3.3.3.1 Ni Anchored α-SiX (X = N, P, As, Sb and Bi) Monolayers as SACs

The binding energy (E_b) stands as a critically significant parameter governing the viability of utilizing any SACs in repetitive application. In our study, we have calculated the E_b of transition metals when they are anchored onto the designated support. This anchoring process leads to the formation of SACs. The computation of E_b has been performed using the subsequent relation[10-15]:

$$E_b = E(\text{Transition Metal} + \text{System}) - E(\text{System}) - E(\text{Transition Metal}) \text{ -----(3.4)}$$

where E(Transition Metal + System) represents the total energy of the transition metal anchored within the considered system and E(Transition Metal) represents the total energy of the isolated transition metal.

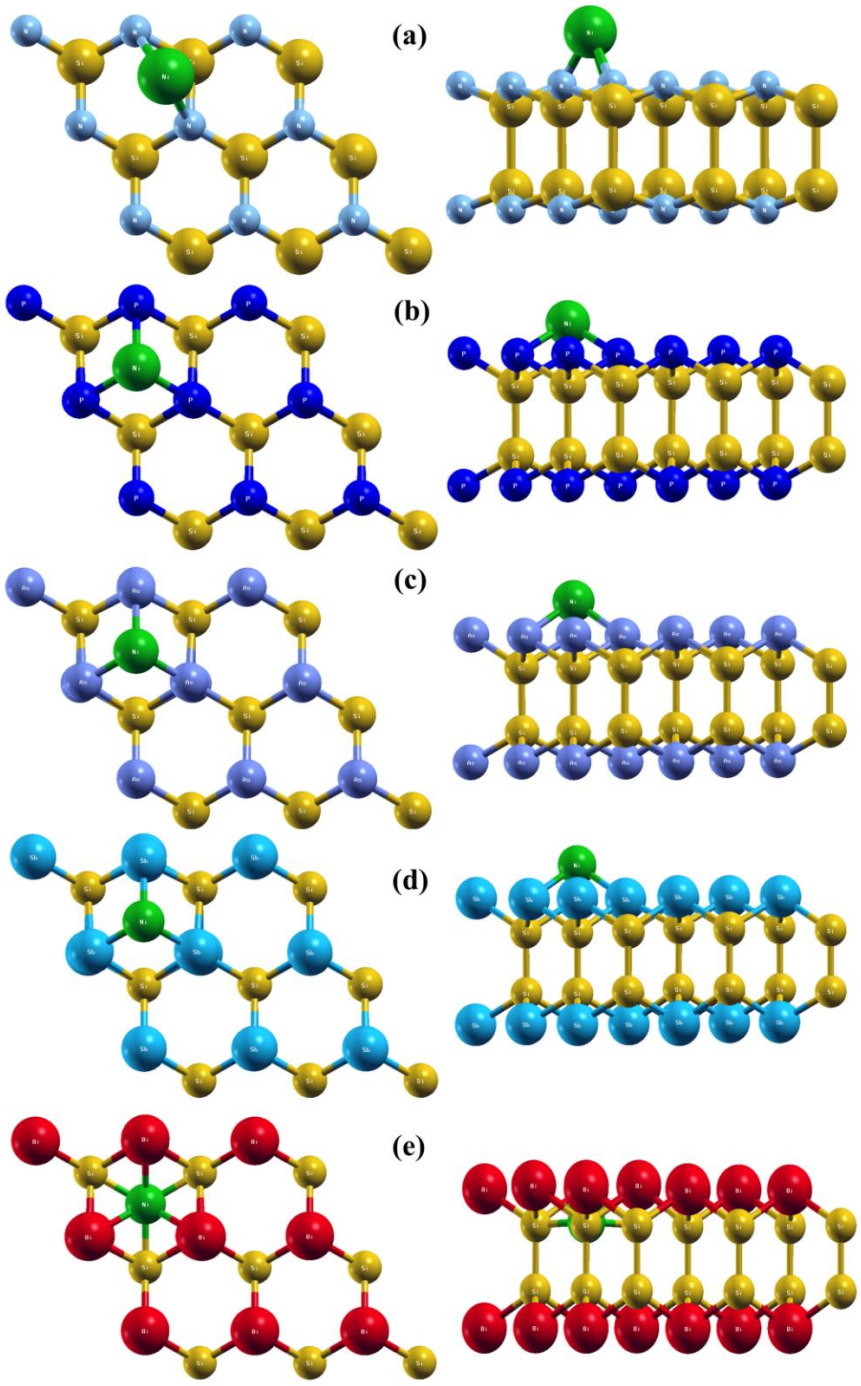

Figure 3.4: Structural geometry of Ni@α-SiN (a), Ni@α-SiP (b), Ni@α-SiAs (c), Ni@α-SiSb (d) and Ni@α-SiBi (e) SACs. The green sphere represents the Ni atom.

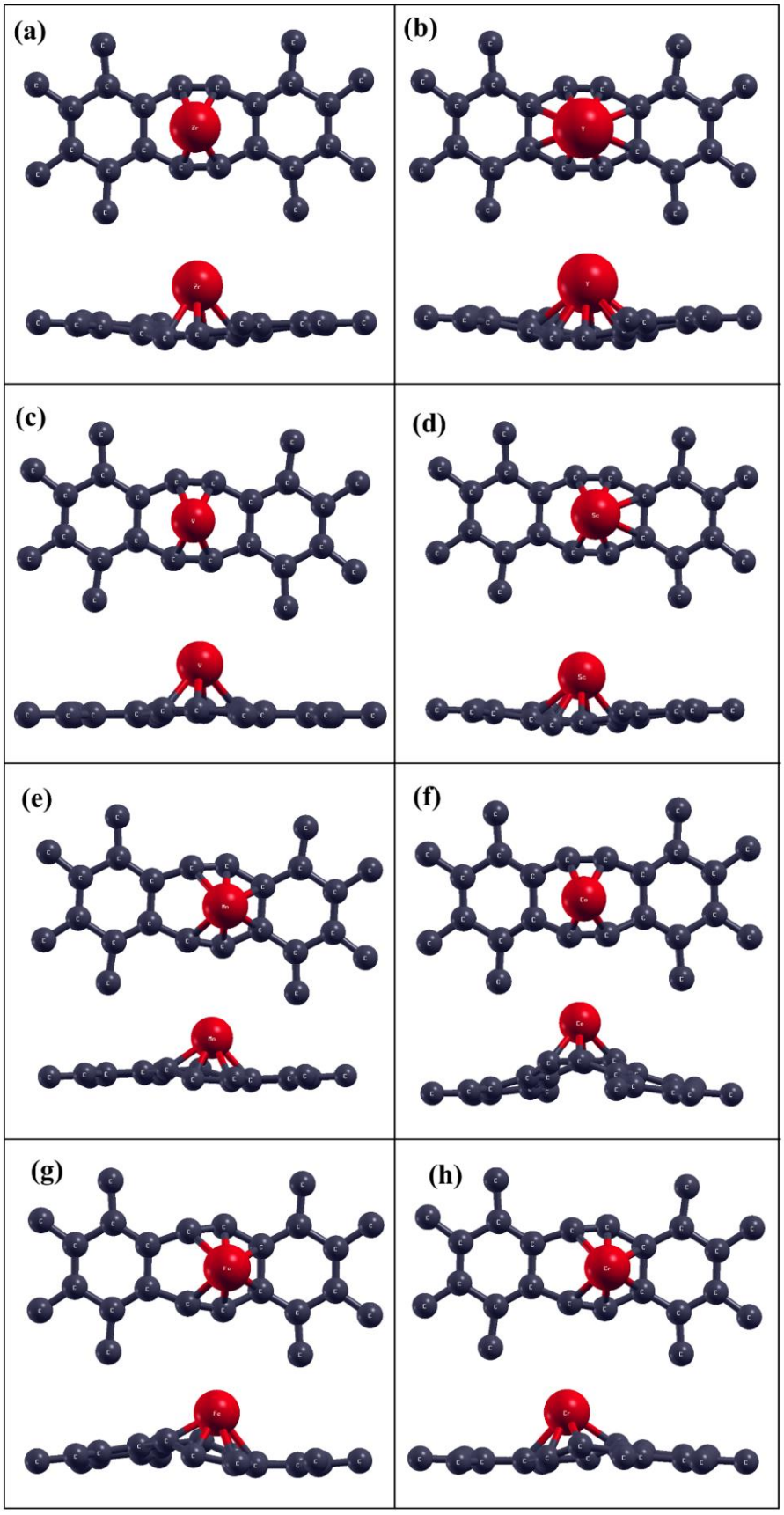

Figure 3.5: Structural geometry of Zr@HGY (a), Y@HGY (b), V@HGY (c), Sc@HGY (d), Mn@HGY (e), Co@HGY (f), Fe@HGY (g) and Cr@HGY (h)) SACs, respectively.

In the case of α-SiX monolayers, we have examined multiple sites for decorating with Ni atoms. Among these sites, the one with the lowest energy is depicted in Fig. 3.4 and has been selected for further investigation. Using equation (3.4), we have computed E_b of Ni single transition metals as follows: -1.99 eV for α-SiN, -3.79 eV for α-SiP, -3.13 eV for α-SiAs, -3.28 eV for α-SiSb and -5.32 eV for α-SiBi. The consistently negative value of E_b for Ni across all Ni@α-SiX structural configurations underscore the exceptional bonding of the Ni atom when introduced onto the α-SiX substrate. This characteristic underscore the excellent suitability of α-SiX as a substrate for supporting the Ni atom.

3.3.3.2 Transition Metal Anchored HGY Monolayers as SACs

The literature survey reveals that the introduction of various transition metals onto various monolayers enhances their HER activity.[10-16] We have strategically anchored several transition metals (Zr, Y, V, Sc, Mn, Co, Fe, Cr) onto different potential locations of the HGY sheet to enhance the activity of the HER. Notably, we present the lowest energetic configurations, both in top and side views, in Fig. 3.5. In our study, we have calculated E_b of these transition metals supported by the HGY monolayer, employing equation (3.4). The computed E_b values are as follows: -4.72 eV for Zr, -3.57 eV for Y, -5.23 eV for V, -3.60 eV for Sc, -2.50 eV for Mn, -2.44 eV for Co, -2.27 eV for Fe and -5.69 eV for Cr. The consistently negative values of E_b for these transition metals anchored to the HGY support signify a strong binding affinity, suggesting their excellent suitability as catalyst substrates.

3.3.4 Structural Changes and Band Structure Analysis of the SACs

Extensive literature review reveals that the introduction of foreign atoms to the analyzed monolayers drives to significant alterations in its electronic and structural properties. Similarly, when single Ni atom is anchored onto the α-SiX supports and various transition metals are subsequently introduced over the HGY monolayer, considerable changes in electronic and structural traits are observed and thoroughly discussed below:

3.3.4.1 Ni Anchored α-SiX SACs

Table 3.3: Structural parameters and band gap values for Ni@α-SiX SACs with and without H adsorption conditions, respectively.

System	Bond length (Å)				Angle (°)		Band gap (eV)
	Si-Si	X-X	Si-X	TM-H	θ_1 (Si-Si-X)	θ_2 (Si-X-Si)	
Ni@α-SiN	2.38	3.57	1.80	----	111.10	109.63	0.16
H+Ni@α-SiN	2.39	3.54	1.79	1.48	109.13	109.84	Metallic
Ni@α-SiP	2.34	4.32	2.25	----	116.23	104.33	0.59
H+Ni@α-SiP	2.35	4.30	2.28	1.49	113.80	102.38	Metallic
Ni@α-SiAs	2.32	4.52	2.38	----	118.31	102.90	0.26
H+Ni@α-SiAs	2.34	4.51	2.41	1.48	115.65	100.13	Metallic
Ni@α-SiSb	2.32	4.76	2.58	----	119.18	102.28	0.29
H+Ni@α-SiSb	2.32	4.87	2.70	1.53	118.57	94.35	Metallic
Ni@α-SiBi	2.32	4.99	2.74	----	120.49	94.15	0.13
H+Ni@α-SiBi	2.31	5.05	2.78	1.56	121.51	88.83	Metallic

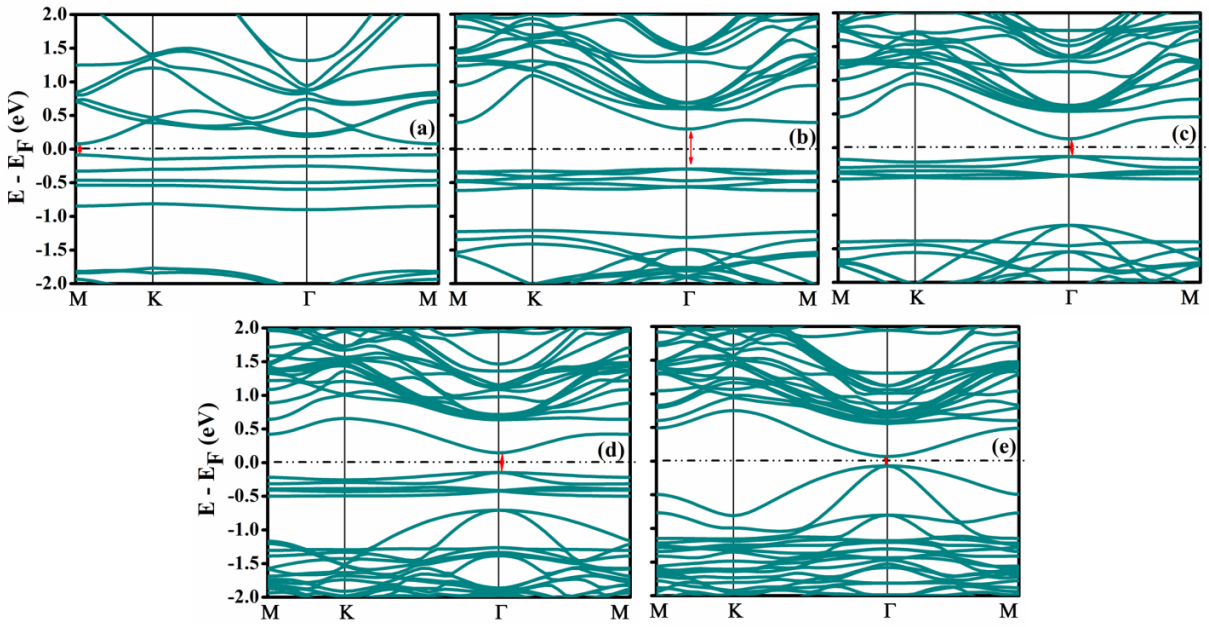

Figure 3.6: Band structure of Ni@α-SiN (a), Ni@α-SiP (b), Ni@α-SiAs (c), Ni@α-SiSb (d) and Ni@α-SiBi (e) SACs, respectively.

Alterations in the structural parameters of Ni@α-SiX SACs are outlined in Table 3.3. The integration of a single Ni atom into the α-SiX supports induces reasonable structural adjustments within the α-SiX monolayers. This outcome can be attributed to the robust interaction between the Ni atom and the α-SiX support. In the case of Ni@SiX (X=N, Bi), the Ni atom is positioned at an average distance of 2.27 Å (or 2.06 Å) and 2.32 Å (or 2.73 Å) from the Si (or X=N, Bi) atoms, respectively. This configuration clearly demonstrates bonding between the Ni atom and its support (depicted in Fig. 3.4(a, e)). Similarly, in the context of Ni@SiX (X=P, As, Sb), the Ni single atom is situated at distances of 2.23 Å, 2.38 Å and 2.53 Å from the X atoms, respectively, showcasing evident bonding between them (illustrated in Fig. 3.4(b, c, d)). The observed bonding between the Ni single atom and Si or X (=N, P, As, Sb, Bi) atoms align consistently with the obtained E_b values.

The band gaps of Ni@α-SiX SACs reduce significantly to 0.16 eV, 0.59 eV, 0.26 eV, 0.29 eV and 0.13 eV from their respective pristine monolayer values of 1.75 eV, 1.50 eV, 1.57 eV, 1.13 eV and 0.78 eV, marking reductions of 90.85%, 60.66%, 83.43%, 74.33% and 83.33%, respectively (see Fig. 3.6). For Ni@α-SiN SAC, the band gap transition shifts from an indirect (at MK to M high symmetry point of the BZ, Fig. 3.2(a)) to a direct transition (at M point of the BZ, Fig. 3.6(a)). For Ni@α-SiX (X=P, As, Sb) SACs, the Ni single atom induces a shift from indirect (ΓK to M for α-SiP, Γ to M for α-SiAs, and Γ to M for α-SiSb, Fig. 3.2(c, e, g)) to direct band gap transitions at the Γ point of the BZ (Fig. 3.6(b, c, d)). In Ni@α-SiBi (Fig. 6(f)), the band gap reduces while remaining directly positioned at the Γ point of the BZ. This transition from indirect to direct band gap in Ni@α-SiX (X=N, P, As, Sb) SACs open their optoelectronic applications[35,36], and the decreased band gap upon Ni single atom introduction boosts electrical conductivity of its support.

3.3.4.2 Transition Metals Anchored HGY SACs

Table 3.4: Structural parameters and band gap values for transition metals anchored HGY SACs with and without H adsorption conditions, respectively.

System	Band gap (eV)	Bond length (Å)						ø (°)
		L1	L2	L3	L4	Metal-C	Metal-H	
Zr@HGY	0.37	1.26	1.41	1.47	1.40	2.25	-----	125.16
H+Zr@HGY	Metallic	1.25	1.40	1.48	1.41	2.29	1.89	124.85
Y@HGY	Metallic	1.25	1.40	1.48	1.42	2.46	-----	125.09
H+Y@HGY	Metallic	1.24	1.39	1.49	1.41	2.60	1.95	125.24
V@HGY	Metallic	1.26	1.41	1.46	1.40	2.07	-----	125.59
H+V@HGY	0.73	1.26	1.42	1.46	1.39	2.11	1.73	126.53
Sc@HGY	Metallic	1.24	1.40	1.48	1.41	2.35	-----	124.93
H+Sc@HGY	Metallic	1.24	1.39	1.48	1.40	2.36	1.82	124.87
Mn@HGY	Metallic	1.26	1.41	1.48	1.41	2.09	-----	123.86
H+Mn@HGY	0.75	1.25	1.40	1.48	1.41	2.15	1.61	125.26
Co@HGY	Metallic	1.27	1.41	1.44	1.38	1.98	-----	127.57
H+Co@HGY	0.47	1.25	1.40	1.44	1.37	2.03	1.51	127.06
Fe@HGY	0.31	1.27	1.41	1.46	1.40	2.04	-----	122.81
H+Fe@HGY	Metallic	1.25	1.40	1.47	1.40	2.13	1.55	124.17
Cr@HGY	0.47	1.27	1.40	1.50	1.42	2.10	-----	124.67
H+Cr@HGY	Metallic	1.27	1.42	1.45	1.38	2.02	1.66	127.86

The introduction of transition metals to the HGY support induces predictable structural modifications in the HGY monolayer. These alterations can be attributed to an interaction occurring between the transition metals and HGY support, as outlined in Table 3.4. When transition metals are anchored onto the HGY, they exhibit an average distance of approximately 2.25 Å, 2.46 Å, 2.07 Å, 2.35 Å, 2.09 Å, 1.98 Å, 2.04 Å and 2.10 Å from the C atoms of the HGY support. This distinctive proximity highlights a discernible and robust binding between the transition metals and the HGY, clearly evident in the observed outcomes.

The band gaps of the HGY supports anchored with Zr, Fe and Cr demonstrate reductions of 27.45% (see Fig. 3.7(a)), 39.21% (see Fig. 3.7(g)) and 7.84% (see Fig. 3.7(h)), respectively, compared to their pristine counterparts (see Table 3.4). Furthermore, the other systems involving Y, V, Sc, Mn and Co anchored HGY shift from a semiconducting state to a metallic state (see Fig. 3.7(b-f)). The decrease in the band gap of the HGY support upon the introduction of transition metals has the potential to enhance electrical conductivity of its support.

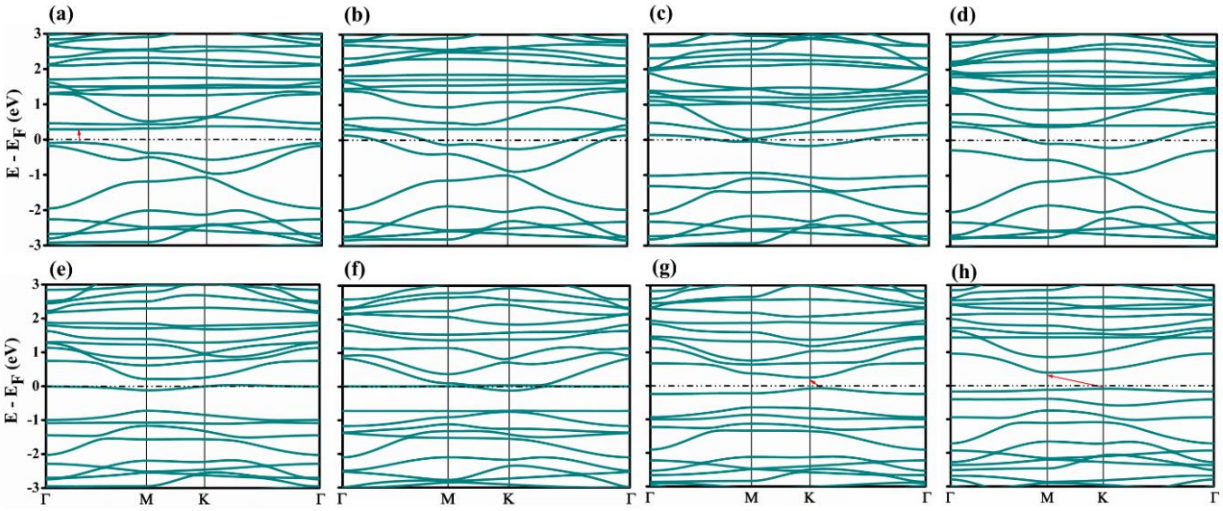

Figure 3.7: Band structure of Zr@HGY (a), Y@HGY (b), V@HGY (c), Sc@HGY (d), Mn@HGY (e), Co@HGY (f), Fe@HGY (g) and Cr@HGY (h) SACs, respectively.

3.3.5 PDOS and Charge Transfer Analysis of the SACs

3.3.5.1 Ni Anchored α-SiX (X = N, P, As, Sb and Bi) SACs

To investigate further the bonding of a single Ni atom with α-SiX supports and understand the resulting orbital interactions and charge transfer, we conducted a study utilizing PDOS (see Fig. 3.8) and the Löwdin charge transfer analysis (refer to Table 3.5) for SACs. Our examination of Ni@α-SiN SACs revealed that the intensity of the Ni-3d orbital can be separated into bonding and non-bonding states, with the main contribution arising from the bonding state, which correlates well with the calculated E_b value. We also identified hybridization between the Ni-3d orbital and the N-2p (and Si-3p) orbitals (see Fig. 3.8(a)).

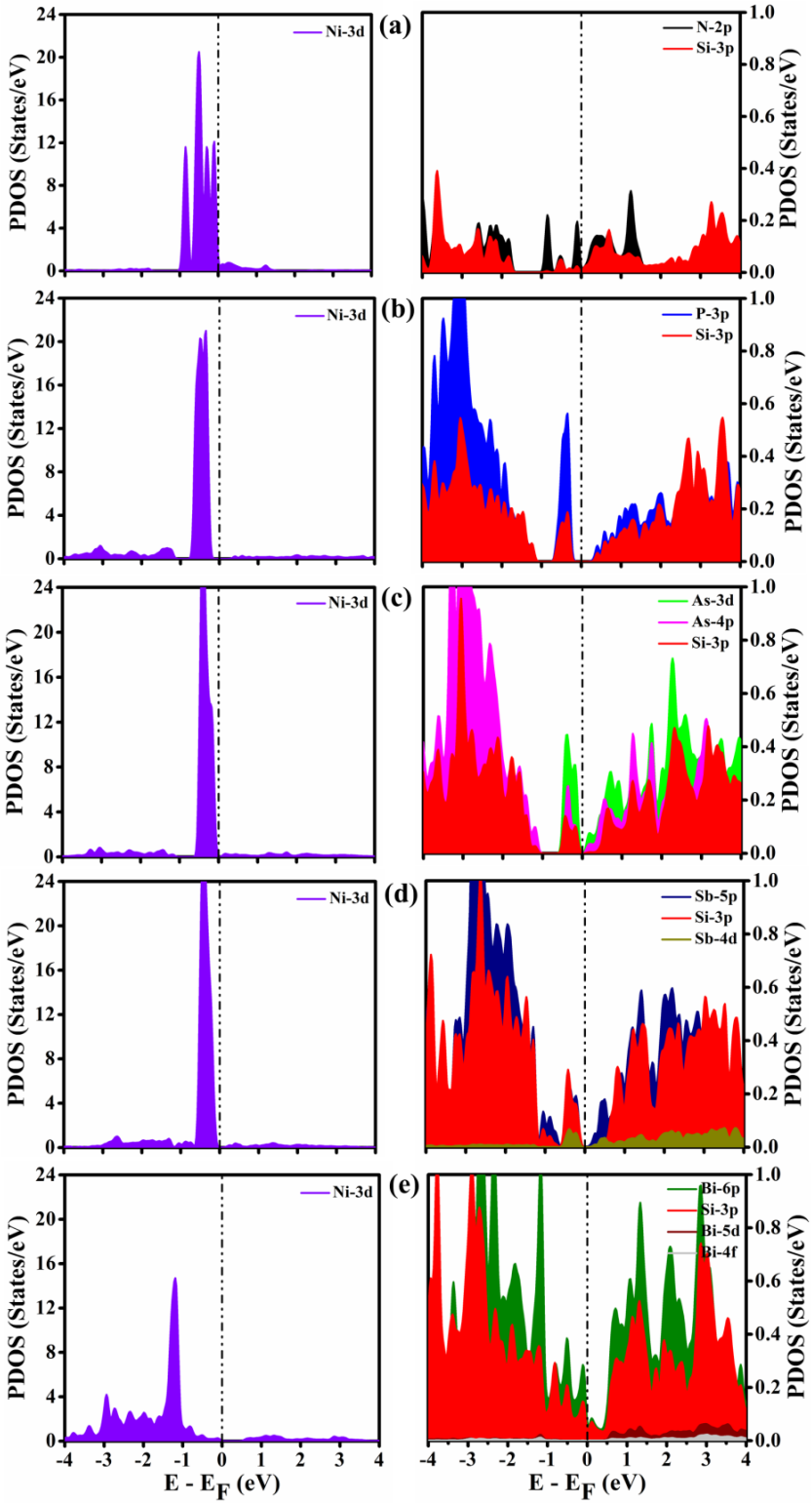

Figure 3.8: PDOS of Ni@α-SiN (a), Ni@α-SiP (b), Ni@α-SiAs (c), Ni@α-SiSb (d) and Ni@α-SiBi (e) SACs, respectively.

Table 3.5: Löwdin charge (e) analysis of pristine α-SiX (X=N, P, As, Sb, Bi), Ni@α-SiX SACs and H adsorbed Ni@α-SiX SACs, respectively.

System	Löwdin charge (e)			
	Si Site	X Site	Ni Site	H Site
Isolated H atom	-----	-----	-----	1.0000
Isolated Ni atom	-----	-----	9.9416	-----
α-SiN	3.4218	5.5612	-----	-----
Ni@α-SiN	3.4348	5.5869	9.2637	-----
H+Ni@α-SiN	3.4220	5.5795	9.2392	1.3492
α-SiP	4.1376	4.8365	-----	-----
Ni@α-SiP	4.1409	4.8667	9.3546	-----
H+Ni@α-SiP	4.1405	4.8494	9.2490	1.4382
α-SiAs	4.0277	4.9500	-----	-----
Ni@α-SiAs	4.0271	4.9815	9.4022	-----
H+Ni@α-SiAs	4.0269	4.9663	9.2845	1.4239
α-SiSb	4.6760	4.2938	-----	-----
Ni@α-SiSb	4.6802	4.2994	9.7155	-----
H+Ni@α-SiSb	4.6799	4.2755	9.3210	1.7327
α-SiBi	4.6305	4.3436	-----	-----
Ni@α-SiBi	4.6586	4.3488	9.3588	-----
H+Ni@α-SiBi	4.6251	4.3209	9.3218	1.8182

We noticed a reduction in the intensity of Ni-3d orbitals near the E_F as compared to isolated Ni-3d orbitals (which contribute only at E_F), indicating a loss of charge from the Ni atom's 3d orbital upon interaction with the α-SiN support. Importantly, we observed the emergence of electronic states near E_F for both bonding and anti-bonding states of Si-3p and N-2p orbitals (as illustrated in Fig. 3.8(a)), a phenomenon absents in the pristine α-SiN state (as shown in Fig. 3.2(b)). This newly identified state near E_F in Si-3p and N-2p orbitals signifies a transfer of charge from the Ni atom's 3d orbitals to the Si-3p and N-2p orbitals due to the

interaction between the Ni single atom and the α-SiN support. Furthermore, the increase in Löwdin charge (detailed in Table 3.5) for Si and N atoms (3.4348e and 5.5869e) in the Ni@α-SiN SAC, in comparison to the pristine α-SiN monolayer (3.4218e and 5.5612e), leads to a reduction in the band gap. Additionally, a decrease in Löwdin charge is observed on the Ni atom (9.2637e) of Ni@α-SiN when compared to the isolated Ni atom (9.9416e), which is consistent with the findings from the PDOS analysis. The qualitative analysis of charge transfer derived from the PDOS aligns with the quantitative analysis of Löwdin charges.

Similar to Ni@α-SiN SAC, we find that Ni@α-SiX (X = P, As, Sb, Bi) also exhibits the split of Ni-3d orbital intensity into bonding and non-bonding states (see Fig. 3.8). The bonding state is dominant by Ni-3d orbitals, aligning with calculated E_b. Hybridization between Ni-3d and host orbitals (N-2p, Si-3p for Ni@α-SiN; As-4d, Si-3p, As-4p for Ni@α-SiAs; Sb-5p, Si-3p, Sb-4d for Ni@α-SiSb; Bi-6p, Si-3p for Ni@α-SiBi) is observed close to E_F. Ni-3d orbital intensity near E_F decreases compared to the isolated Ni, implying charge loss from Ni atom upon interaction with α-SiX. New electronic states appear near E_F of host orbitals in Ni@α-SiX compared to pristine α-SiX materials. Löwdin charge analysis shows increased charges on Si and X atoms in Ni@α-SiX, responsible for the reduction in band gap. Ni@α-SiX exhibits reduced Ni charge compared to isolated Ni, consistent with PDOS analysis, indicating Ni single atom donates Löwdin charge to host material. In general, a Ni single atom anchored onto a monolayer tends to donate its Löwdin charge to the host material's atoms due to its lower electronegativity compared to the host material's atoms.[37] Hence, PDOS and charge analysis also prove the modification in the electronic properties after the introduction of the foreign atom to the host material.

3.3.5.2 Transition Metals Anchored HGY SACs

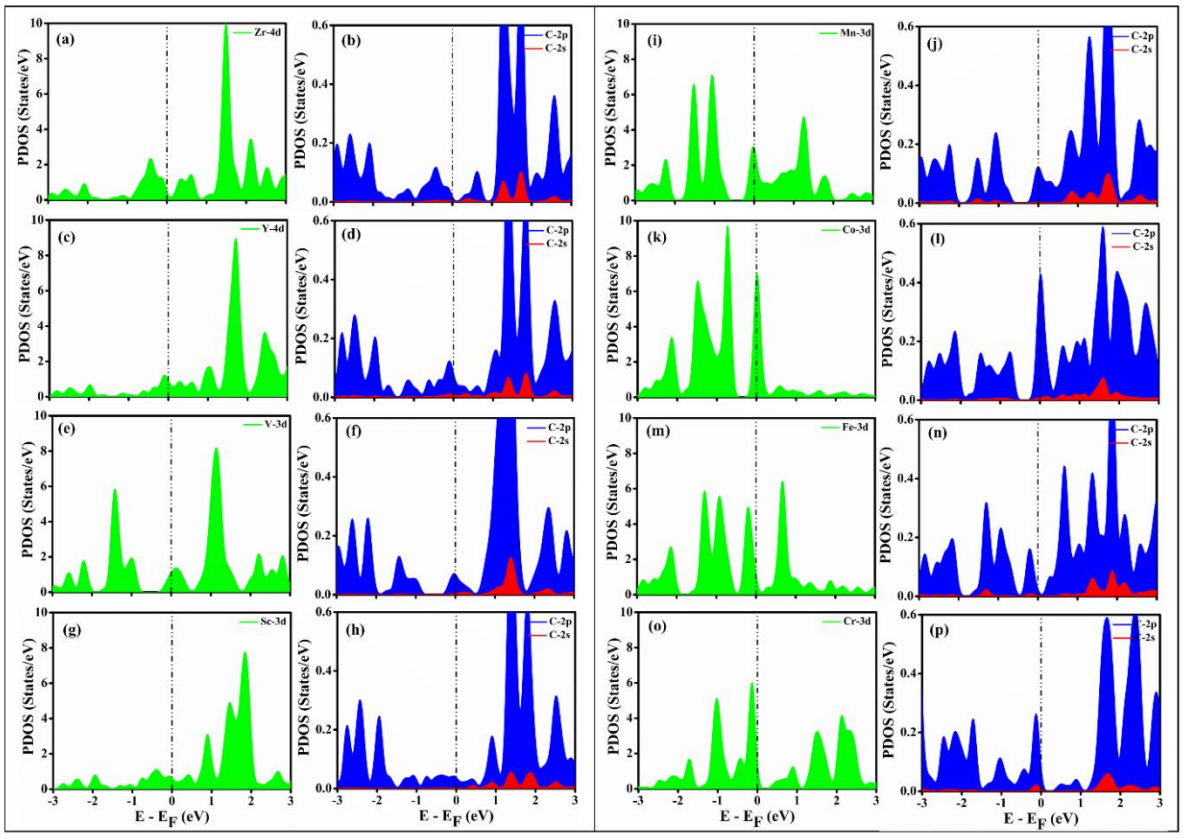

Figure 3.9: PDOS analysis of Zr@HGY (a, b), Y@HGY (c, d), V@HGY (e, f), Sc@HGY (g, h), Mn@HGY (i, j), Co@HGY (k, l), Fe@HGY (m, n) and Cr@HGY (o, p) SACs, respectively.

To verify the interaction between transition metals and HGY monolayer, we extensively examined PDOS (refer to Fig. 3.9) and analysed Löwdin charge transfer (refer to Table 3.6). Isolated Zr's Zr-4d orbital only contributes at E_F. For Zr@HGY SAC, the Zr-4d orbital splits into bonding/non-bonding states (see Fig. 3.9(a)), hybridizing with C-2p/-2s (see Fig. 3.9(b)). The reduced peak intensity near E_F (as compared to the isolated Zr atom) suggests that the Zr-4d donates charge to HGY, evident by new C-2p/-2s states at E_F (Fig. 3.9(b)). Charge accumulates on C atoms (4.0250e) of Zr@HGY SAC as compared to pristine HGY (3.9872e), reducing the band gap. Reduced Löwdin charge on Zr (3.0826e) aligns with PDOS. Consistency between analysis from PDOS and Löwdin charge transfer is noteworthy.

Table 3.6: The Löwdin charge analysis of the pristine, transition metals anchored HGY and H adsorbed transition metals anchored HGY, respectively.

System	Average Löwdin charge (e)		
	C	Metal	H
Isolated H atom	-----	-----	1.0000
HGY	3.9872	-----	-----
Isolated Zr atom	-----	3.9980	-----
Zr@HGY	4.0250	3.0826	-----
H+Zr@HGY	4.0166	3.0394	1.2366
Isolated Y atom	-----	2.9952	-----
Y@HGY	4.0283	2.0027	-----
H+Y@HGY	4.0173	2.0260	1.2387
Isolated V atom	-----	4.9955	-----
V@HGY	4.0223	4.1582	-----
H+V@HGY	4.0074	4.2789	1.2292
Isolated Sc atom	-----	2.9980	-----
Sc@HGY	4.0280	2.0261	-----
H+Sc@HGY	4.0129	2.1434	1.2383
Isolated Mn atom	-----	6.9752	-----
Mn@HGY	4.0198	6.2146	-----
H+Mn@HGY	4.0096	6.3306	1.1245
Isolated Co atom	-----	8.9714	-----
Co@HGY	4.0123	8.3859	-----
H+Co@HGY	4.0038	8.4968	1.0886
Isolated Fe atom	-----	7.9981	-----
Fe@HGY	4.0159	7.3061	-----
H+Fe@HGY	4.0106	7.3530	1.0765
Isolated Cr atom	-----	5.9813	-----
Cr@HGY	4.0140	5.3522	-----
H+Cr@HGY	4.0022	5.4647	1.1491

For isolated transition metals (Y, V, Sc, Mn, Co, Fe, Cr), d orbitals majorly contribute at E_F. Anchoring transition metals to HGY divides d orbitals into bonding and non-bonding (Fig. 3.9), hybridizing with C-2p/-2s. Reduced d orbital intensity compared to d orbital of isolated metals near E_F signifies the charge donation to HGY. Appearance of C-2p/-2s near E_F, absent in pristine HGY, confirms charge gain. Reduced charge (see Table 3.6) on transition metals after interaction matches PDOS (see Fig. 3.9). The harmony between "qualitative charge transfer analysis from PDOS" and "quantitative charge transfer from Löwdin charge analysis"

holds. The lower electronegativity of transition metals compared to carbon atom results in the donation of charges to the carbon atoms of HGY. [37]

3.3.6 HER Activity over the SACs

In order to attain a comprehensive understanding of the catalytic performance regarding the HER activity of the aforementioned SACs, our initial approach entailed positioning the H atom 2 Å above each individual transition metals. Following this, we carried out optimization of the structure to gain a more profound insight into the behavior of the systems.

Table 3.7: The obtained adsorption energy and Gibbs free energy of the SACs for HER activity.

System	ΔE_{ads}^{H} (eV)	ΔG_H (eV)
H+Ni@α-SiN	-0.28	-0.04
H+Ni@α-SiP	0.51	0.75
H+Ni@α-SiAs	0.25	0.49
H+Ni@α-SiSb	-0.91	-0.67
H+Ni@α-SiBi	0.80	1.04
H+Zr@HGY	-1.01	-0.77
H+Y@HGY	-0.92	-0.68
H+V@HGY	-0.82	-0.58
H+Sc@HGY	-0.70	-0.46
H+Mn@HGY	-0.70	-0.46
H+Co@HGY	-0.45	-0.21
H+Fe@HGY	-0.38	-0.14
H+Cr@HGY	-0.29	-0.05

3.3.6.1 HER Activity over Ni Anchored α-SiX (X = N, P, As, Sb and Bi) SACs

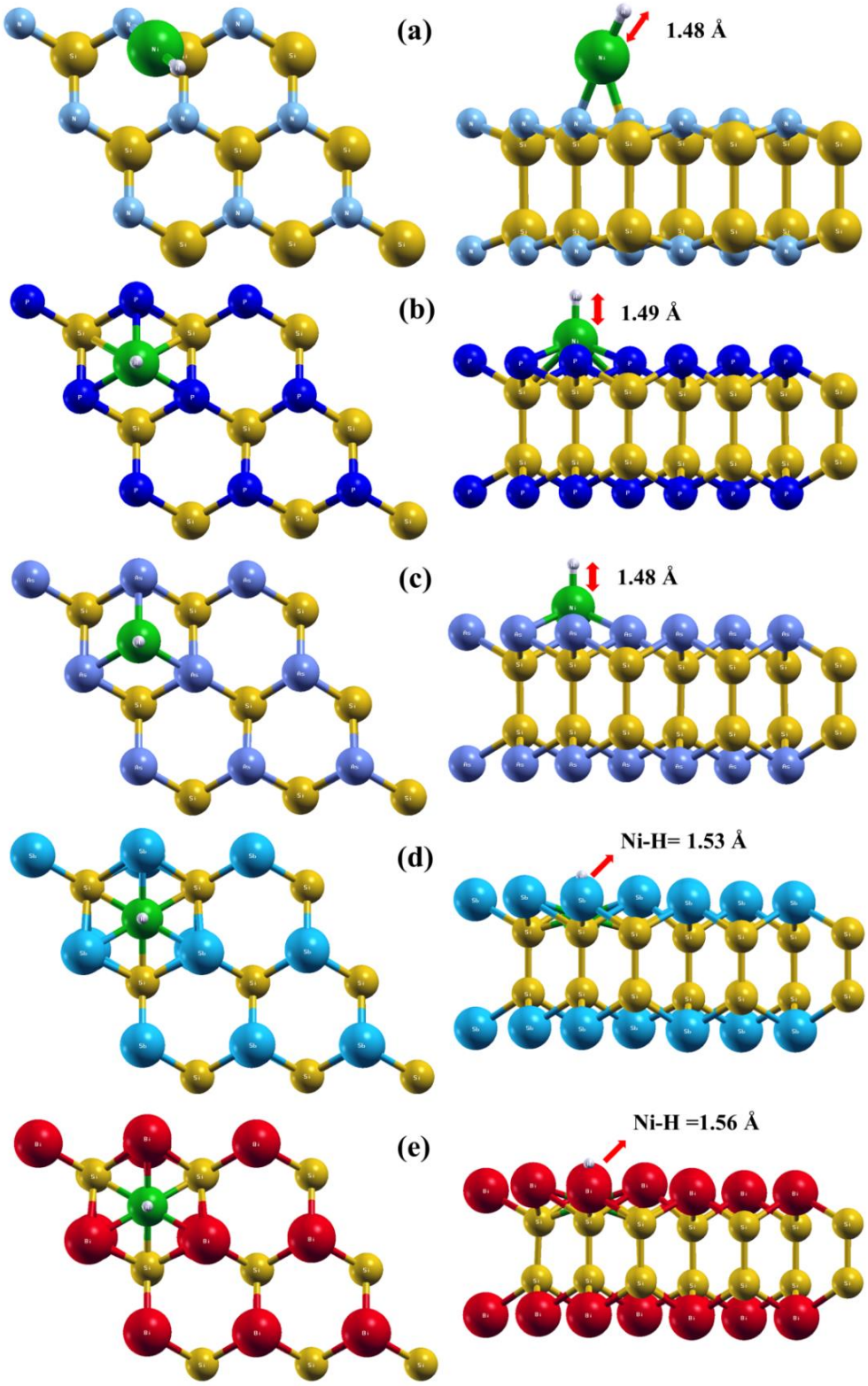

Figure 3.10: Structural geometry of the H adsorbed over Ni@α-SiN (a), Ni@α-SiP (b), Ni@α-SiAs (c), Ni@α-SiSb (d) and Ni@α-SiBi (e) SACs, respectively.

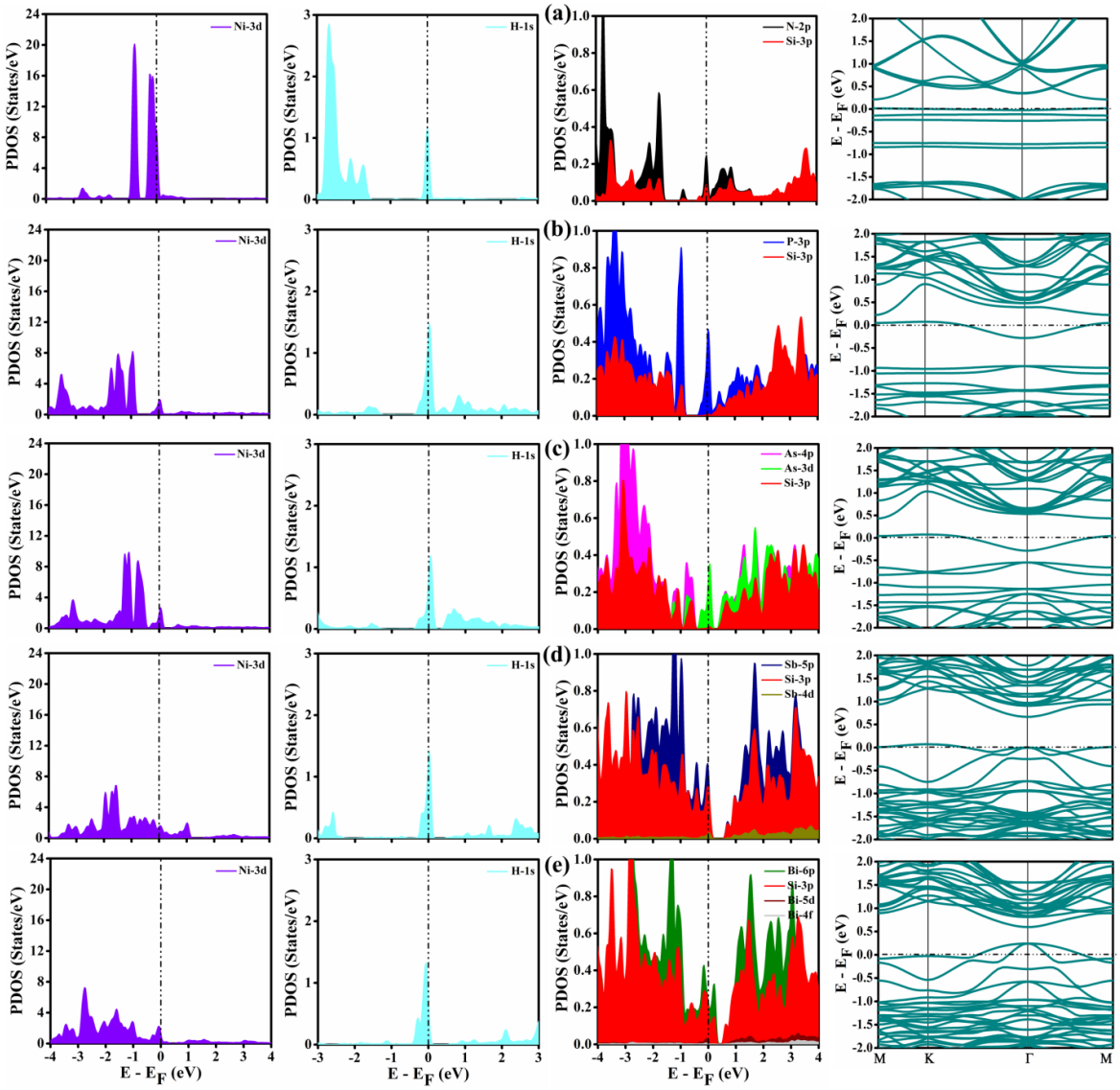

Figure 3.11: PDOS and band structure of the H adsorbed over Ni@α-SiN (a), Ni@α-SiP (b), Ni@α-SiAs (c), Ni@α-SiSb (d) and Ni@α-SiBi (e) SACs, respectively.

The variation in structural parameters concerning H adsorbed Ni@α-SiX SACs and Ni@α-SiX SACs have been compiled in Table 3.3 to facilitate comparison. Following the relaxation process, the separation between the H atom and the Ni single atom within the SACs is determined to be 1.48 Å, 1.49 Å, 1.48 Å, 1.53 Å and 1.56 Å, respectively (refer to Fig. 3.10 and Table 3.3 for a visual representation and detailed data). In the context of H adsorbed Ni@α-SiX (X = N, P, As, Sb, Bi) SACs, the Ni single atom experiences an average distance of 2.51 Å (or 2.03 Å), 2.65 Å (or 2.23 Å), 2.37 Å, 2.35 Å (or 2.57 Å) and 2.35 Å (or 2.62 Å) from the

Si (or X = N, P, As, Sb, Bi) atom, respectively. This parameter also exhibits a minor adjustment due to the interplay between H and Ni@α-SiX SACs.

To assess the efficiency of Ni@α-SiX SACs in promoting the catalytic activity for HER, we computed the values of ΔE_{ads}^{H} and ΔG_H using equations (3.1, 3.2 and 3.3), which are presented in Table 3.7. The calculated ΔE_{ads}^{H} (ΔG_H) values are as follows: 0.51 eV (0.75 eV), 0.25 eV (0.49 eV) and 0.80 eV (1.04 eV) for H adsorption on Ni@α-SiX (X=P, As, Bi) SACs, respectively. Notably, the HER activity efficiency shows an increase; however, it is important to acknowledge that the calculated ΔG_H values deviate from the ideal value of 0 eV. Consequently, based on these findings, it is evident that Ni@α-SiX (X=P, As, Bi) SACs are not viable candidates for facilitating the HER activity.

To delve into the HER activity of Ni@α-SiX (X = P, As, Bi) SACs, we have illustrated PDOS and band structures in Fig. 3.11(b, c and e). These visuals highlight the dominant contribution of H-1s orbitals into non-bonding region, indicating hydrogen's physisorption onto Ni@α-SiX (X = P, As, Bi) SACs. The coherence between calculated ΔE_{ads}^{H} and H-1s orbital involvement underscores the unsuitability of Ni@α-SiX (X = P, As, Bi) SACs for catalytic activity of HER. Furthermore, in Fig. 3.11(b, c, e), Ni-3d orbital intensity near the E_F reduces in the bonding state, contrasting with Ni@α-SiX (X = P, As, Bi) SACs (Fig. 3.8(b, c, e)). This suggests charge reduction in Ni's 3d orbital upon H interaction. Furthermore, semiconductor to metal transition is observed due to the presence of Ni-3d orbitals (for Ni@α-SiX (X = P, As, Bi)), P-3p orbitals (for Ni@α-SiP), As-3d orbitals (for Ni@α-SiAs), Si-3p or Bi-6p orbitals (for Ni@α-SiBi) at E_F, as validated by respective band structures (Fig. 3.11). Moreover, Löwdin charge analysis (Table 3.5) reveals reduced charges on Ni, Si and X (X = P, As, Bi) upon H adsorption compared to Ni@α-SiX (X = P, As, Bi) SACs. This consistent trend with PDOS

signifies H acquiring charge from Ni@α-SiX (X = P, As, Bi) SACs, with H gaining 0.4382e, 0.4239e, and 0.8182e from Ni@α-SiX (X = P, As, Bi) SACs respectively.

For the H adsorption onto the Ni@α-SiSb SAC, the calculated values for ΔE_{ads}^{H} (ΔG_H) are -0.91 eV (-0.67 eV), respectively. These values suggest a remarkably strong interaction between the adsorbate and the catalyst surface, implying that the desorption process will likely be challenging in this scenario. Consequently, the Ni@α-SiSb SAC demonstrates unsuitability for efficient HER activity. To understand H's interaction with Ni@α-SiSb SAC, we have analysed PDOS and band structure (Fig. 3.11(d)). H-1s splits into bonding and non-bonding states for Ni@α-SiBi SACs, showing strong interaction. Ni-3d orbital intensity reduces upon H adsorption (Fig. 3.11(d)), indicating charge transfer to H-1s. After H adsorption, the system becomes metallic due to Ni-3d, Sb-5p and Si-3p on E_F, aligning with computed bands (Fig. 3.11(d)). Löwdin charge analysis (Table 3.5) shows reduced charges on Ni, Si, Sb atoms in H adsorbed Ni@α-SiSb SAC, in line with PDOS. H gains 0.7327e charge from Ni@α-SiSb SAC.

Let's now delve into the final outcome regarding Ni@α-SiX SACs, specifically focusing on the adsorption of H over the Ni@α-SiN SAC. In this context, the calculated values for ΔE_{ads}^{H} and ΔG_H stand at -0.28 eV and -0.04 eV, respectively. Remarkably, the Ni@α-SiN SAC demonstrates an optimal ΔG_H value, closely approaching zero. This stands in contrast to both the pristine α-SiX monolayers and the Ni@α-SiX (X = P, As, Sb, Bi) SACs. Such findings strongly suggest that the Ni@α-SiX SAC holds tremendous promise as an exemplary catalyst for driving the HER activity. The analysis of PDOS of H adsorbed Ni@α-SiN SAC reveals a prominent role of the H-1s orbital in the bonding state, aligned with the computed ΔE_{ads}^{H}. The Ni-3d orbital intensity decreases in the bonding state, seen in Fig. 3.11(a) compared to Ni@α-SiN SACs in Fig. 3.8(a), indicating charge transfer to H-1s upon H adsorption and driving a metallic shift. This metallic shift is driven by Ni-3d, N-2p and Si-3p orbitals at E_F, consistent

with the computed band structure in Fig. 3.11(a). Löwdin charge analysis in Table 3.5 confirms these trends: Si, N and Ni atoms lose charge, while H gains a substantial charge of 0.3492e from Ni@α-SiN SAC.

3.3.6.2 HER Activity over Transition Metals Anchored HGY SACs

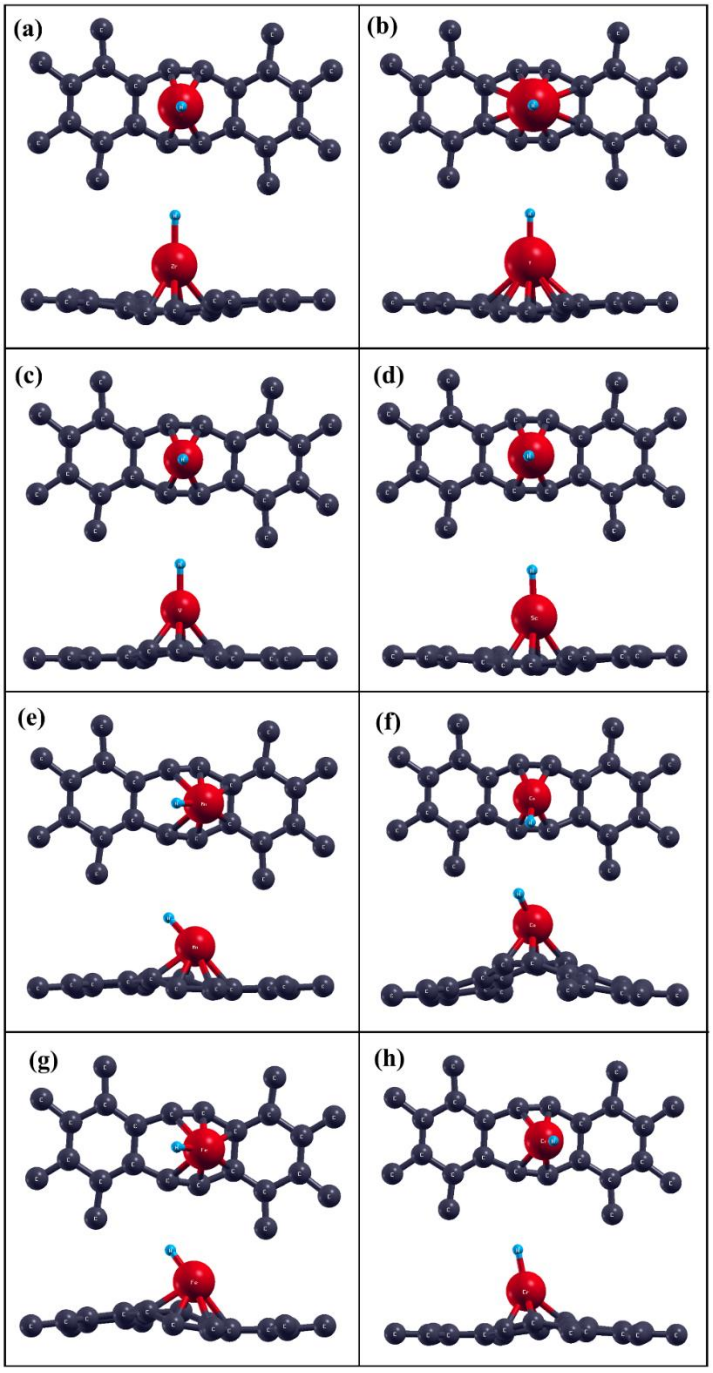

Figure 3.12: Structural geometry of the H adsorbed over Zr@HGY (a), Y@HGY (b), V@HGY (c), Sc@HGY (d), Mn@HGY (e), Co@HGY (f), Fe@HGY (g) and Cr@HGY (h) SACs, respectively.

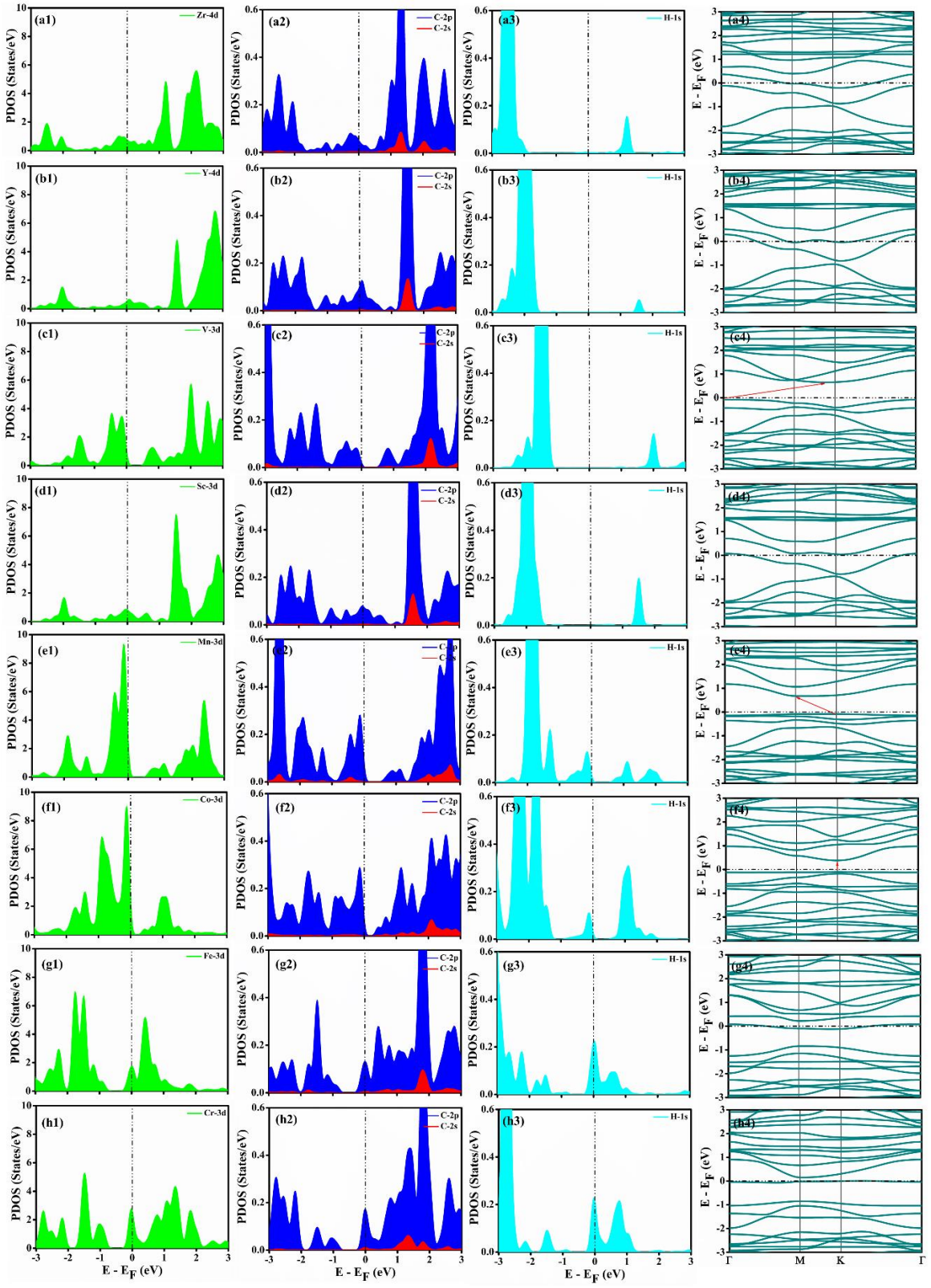

Figure 3.13: PDOS and band structure of the H adsorbed over Zr@HGY (a1-a4), Y@HGY (b1-b4), V@HGY (c1-c4), Sc@HGY (d1-d4), Mn@HGY (e1-e4), Co@HGY (f1-f4), Fe@HGY (g1-g4) and Cr@HGY (h1-h4) SACs, respectively.

Fig. 3.12 displays structural geometry of the H adsorption on transition metals (Zr, Y, V, Sc, Mn, Co, Fe and Cr) anchored to the HGY support. The introduction of H induces slight changes in structural parameters like bond lengths and angles in the transition metals anchored HGY SACs, attributed due to interactions. For comparison, alterations in structural parameters are tabulated in Table 3.4 for H adsorbed transition metals anchored HGY SACs and non-adsorbed counterparts. The H atom distance is 1.89 Å from Zr, 1.95 Å from Y, 1.73 Å from V, 1.82 Å from Sc, 1.61 Å from Mn, 1.51 Å from Co, 1.55 Å from Fe and 1.66 Å from Cr atom of SACs. In H adsorbed scenario, average distance between transition metal and C is 2.29 Å for Zr@HGY, 2.60 Å for Y@HGY, 2.11 Å for V@HGY, 2.36 Å for Sc@HGY, 2.15 Å for Mn@HGY, 2.03 Å Co@HGY, 2.13 Å Fe@HGY and 2.02 Å for Cr@HGY, changed by H interactions, affecting atomic arrangement.

To assess effectiveness of transition metals anchored HGY SACs in HER activity, we computed ΔE_{ads}^{H} and ΔG_H using equations (3.1, 3.2, 3.3), presenting the results in Table 3.7. The calculated ΔE_{ads}^{H} (ΔG_H) values are -1.01 eV (-0.77 eV), -0.92 eV (-0.68 eV), -0.82 eV (-0.58 eV), -0.70 eV (-0.46 eV) and -0.70 eV (-0.46 eV) for H adsorption on Zr, Y, V, Sc and Mn anchored HGY SACs. However, the notably negative ΔE_{ads}^{H} values hinder desorption step during reaction and the significant deviation from the ideal value suggests unsuitability for effective HER activity. Thus, Zr, Y, V, Sc and Mn anchored HGY SACs are inadequate for the intended purpose.

Furthermore, the PDOS and band structures of H adsorbed Zr, Y, V, Sc and Mn anchored HGY were analysed (Fig. 3.13). The H adsorption on Zr@HGY induces a semiconducting to metallic transition due to Zr-4d and C-2p orbitals at E_F (Fig. 3.13(a1 and a2)). This metallic behaviour aligns with the band structure (Fig. 3.13(a4)). H-1s orbital significantly contributes

to bonding states, consistent with ΔE_{ads}^{H} and strong interaction (Fig. 3.13(a3)). H gains 0.2366e charge from Zr@ HGY SAC (see Table 3.6).

The adsorption of H on Y@HGY and Sc@HGY SACs maintains the system's metallic state, primarily driven by the influence of Y's and Sc's d orbitals (Fig. 3.13(b1, b2, d1 and d2)) and augmented by the presence of C's p orbitals on E_F. In addition, metallic behaviour also confirmed by band structure (Fig. 3.13(b4 and d4)). The H-1s orbital dominates the bonding states upon H adsorption, akin to Zr@HGY, indicating strong interaction (see Fig. 5(b3 and d4)). From Table 3.6, Löwdin charge analysis confirms H gains charge from Y@HGY and Sc@HGY SACs.

For H adsorption on V@HGY and Mn@HGY SACs, a shift from metallic to semiconducting occurs. Diminished availability of V's d orbitals (Fig. 3.13(c1)) and Mn's d orbitals (Fig. 3.13(e1)) along with C's p orbitals (Fig. 3.13(c2) and Fig. 3.13(e2)) near E_F level explains the shift. Band structure (Fig. 3.13(c4) and Fig. 5(e4)) shows H adsorption leads to band gaps of 0.73 eV and 0.75 eV (consistent with PDOS). H-1s orbital plays a crucial role in bonding states, implying strong interaction (Fig. 3.13(c3) and Fig. 3.13(e3)). Löwdin charge analysis (Table 3.6) indicates H gains 0.2292e and 0.1245e charge from Y@HGY and Sc@HGY SACs.

Let's shift our focus to the remaining scenarios involving H adsorption onto Co@HGY, Fe@HGY and Cr@HGY SACs. The computed ΔE_{ads}^{H} (ΔG_H) values for these cases are as follows: -0.45 eV (-0.21 eV) for Co@HGY, -0.38 eV (-0.14 eV) for Fe@HGY and -0.29 eV (-0.05 eV) for Cr@HGY SACs. These values indicate that the energy required for H adsorption onto mentioned SACs is relatively modest. In contrast, the calculated ΔE_{ads}^{H} values for Co, Fe and Cr anchored HGY SACs are lower compared to those for Zr, Y, V, Sc and Mn anchored HGY SACs. This observation suggests an optimally balanced interaction - neither excessively

strong nor overly weak. Such a finely tuned interaction is a fundamental prerequisite for achieving remarkable HER activity. Furthermore, the proximity of ΔG_H values to 0 eV underscores the favourable suitability of these systems for demonstrating desirable HER performance. Upon H adsorption on Co@HGY SACs, the system shifts from metallic to semiconducting due to depletion of d orbital of Co atom (Fig. 3.13(f1)) and p orbital of C atoms (Fig. 3.13(f2)) on E_F. This behaviour mirrors the trend seen in H adsorbed V@HGY and Mn@ HGY SACs. The band structure plot (Fig. 3.14(f4)) confirms a calculated band gap of 0.47 eV for the H adsorbed Co@ HGY SAC, aligning with the findings from the PDOS plot. H adsorption on Fe@HGY and Cr@HGY SACs shifts semiconducting systems to metallic. This shift towards metallic behaviour is attributed to the presence of d orbitals of Fe (see Fig. 3.13(g1)) and Cr atoms (see Fig. 3.13(h1)), p orbitals of C atoms (see Fig. 3.13(g2 and h2)) and s orbitals in the H atom (see Fig. 3.13(g3 and h3)) at E_F. These observations are in concurrence with the band structure analysis illustrated in Fig. 3.13(g4 and h4). For H adsorption on Co@HGY, Fe@HGY and Cr@HGY SACs, the H-1s orbitals split into bonding and non-bonding states, displaying significant contributions near E_F, indicative of favourable interactions. Lowdin charge analysis shows Co@HGY, Fe@HGY and Cr@HGY SACs donate 0.0886e, 0.0765e, and 0.1491e charge to H atom (see Table 3.6).

3.3.7 Stability of the SACs from AIMD Simulations

The above study demonstrates the noteworthy HER activity of Ni@α-SiN, Co@HGY, Fe@HGY and Cr@HGY SACs. To assess their practical applicability, it becomes essential to delve into the stability aspect. To evaluate the thermal stability of these SACs under ambient conditions, AIMD simulations were conducted using the NVT ensemble methodology. The simulations were carried out using the VASP code, employing a time step of 1 fs for 5 ps, while maintaining a temperature of 300 K. Notably, there was no substantial migration observed among the transition metal atoms from their initial positions throughout the simulations.

Although minor fluctuations in thermal energy leads to negligible deviations in the bond lengths, the positions of the transition metal atoms remained remarkably consistent with their stable sites (see Fig. 3.14). This observation underscores the robust thermal stability of the SACs and effectively dismisses concerns about potential metal-metal clustering.

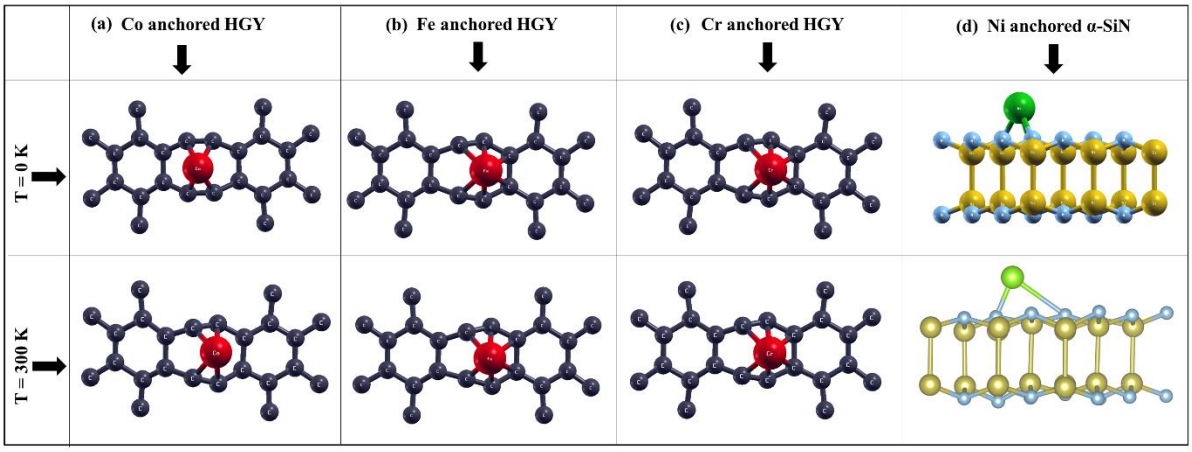

Figure 3.14: Structural geometry of Co@HGY (a), Fe@HGY (b), Cr@HGY (c) and Ni@α-SiN (d) SACs at 0 K and 300 K, respectively.

Table 3.8 The Comparison of calculated Gibbs free energy of HER activity for presented SACs with previous reports.

SACs	ΔG_H (eV)	References
Ni@α-SiN	**-0.04**	**Present work**
Co@HGY	**-0.05**	**Present work**
Co@graphene	0.13	[9]
Cr@silicine	+0.18	[11]
Ni@silicine	+0.13	[11]
Fe@silicine	-0.09	[11]
Ni@graphyne	0.08	[12]
Rh@C_8N_8	0.08	[15]
Mo@C_2N	-0.02	[16]
Ni@C_9N_4	-0.04	[38]
Ni@$B_{12}P_{12}$	-0.06	[39]
Co@$B_{12}P_{12}$	-0.20	[39]
Co@C_{12}	-0.23	[40]
Ni@C_{12}	0.23	[40]
Cu@C_{12}	-0.14	[40]
Ni@Al_6N_6	0.18	[40]
Ni@α-PC	+0.09	[41]

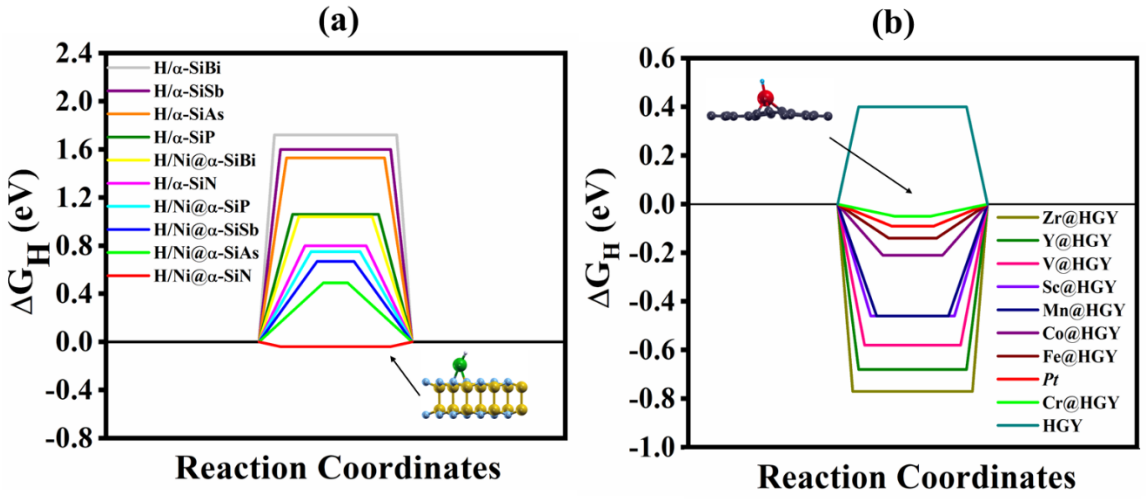

Figure 3.15: The reaction coordinates plot for HER activity of pristine α-SiX (X=N, P, As, Sb, Bi), Ni anchored α-SiX (X=N, P, As, Sb, Bi) SACs, pristine HGY and transition metals (Zr, Y, V, Sc, Mn, Co, Fe, Cr) anchored HGY SACs, respectively.

3.3.8 Drawing Comparison with Previous Studies

In Figure 3.15, we depict the reaction coordinates illustrating the HER activity of pristine α-SiX (X=N, P, As, Sb, Bi), Ni anchored α-SiX (X=N, P, As, Sb, Bi) SACs, pristine HGY and transition metals (Zr, Y, V, Sc, Mn, Co, Fe, Cr) anchored HGY SACs. Analysing Fig. 3.14 (a and b), it becomes evident that Ni@α-SiN and Cr@HGY emerge as highly promising candidates for HER activity within this set. A comparative analysis with previous reports is presented in Table 3.8. The presented study demonstrates that the Ni@α-SiN and Cr@HGY SACs exhibits excellent HER activity compared to Co@graphene, Cr@silicine, Ni@silicine, Fe@silicine, Ni@graphyne, Rh@C_8N_8, Co@$B_{12}P_{12}$, Co@C_{12}, Ni@C_{12}, Cu@C_{12}, Ni@Al_6N_6 and Ni@α-PC SACs, while it shows comparable performance to Mo@C_2N, Ni@C_9N_4 and Ni@$B_{12}P_{12}$ SACs.[9,11,12,15,16,38-41]

3.4 Conclusions

In summary, our study delves into the HER activity of pristine α-SiX (X=N, P, As, Sb, Bi), Ni anchored α-SiX (X=N, P, As, Sb, Bi) SACs, pristine HGY and transition metals (Zr, Y, V, Sc, Mn, Co, Fe, Cr) anchored HGY. This investigation is carried out through comprehensive DFT calculations. We elucidate the alterations in the structural and electronic properties of α-

SiX (X=N, P, As, Sb, Bi) and HGY due to anchoring with transition metals. This is achieved by considering orbital interactions, changes in band structures and PDOS analysis. The robust bonding between Ni metal and α-SiX (X=N, P, As, Sb, Bi) monolayers, as well as between transition metals and HGY monolayer, facilitated by p-d hybridization, enhances reactivity and conductivity. This is further attributed to a decrease in the band gap of the semiconducting α-SiX and HGY monolayers. Our DFT finding predicts that Ni@α-SiX and Cr@HGY SACs emerge as highly efficient catalysts for HER, exhibiting remarkably low ΔG_H values of -0.04 eV and -0.05 eV, respectively. To ascertain stability, we conducted extensive AIMD simulations at 300K, affirming the integrity of Ni@α-SiX and Cr@HGY SACs at room temperature. Given the exceptional electrochemical performance for HER activity and stability of Ni@α-SiX and Cr@HGY SACs, they hold promise as catalysts for hydrogen production. We hold a strong conviction that our theoretical data will serve as inspiration for experimentalists aiming to craft cost-effective, high-performance HER catalysts based on the α-SiN and HGY monolayers.

References

1 D. Strmcnik, P. P. Lopes, B. Genorio, V. R. Stamenkovic and N. M. Markovic, *Nano Energy*, 2016, **29**, 29–36.

2 I. Dincer and C. Acar, *Int. J. Hydrogen Energy*, 2015, **40**, 11094–11111.

3 P. C. K. Vesborg, B. Seger and I. Chorkendorff, *J. Phys. Chem. Lett.*, 2015, **6**, 951–957.

4 D. Chodvadiya, N. N. Som, P. K. Jha and B. Chakraborty, *Int. J. Hydrogen Energy*, 2021, **46**, 22478–22498.

5 Y. Zheng, Y. Jiao, M. Jaroniec and S. Z. Qiao, *Angew. Chemie - Int. Ed.*, 2015, **54**, 52–65.

6 Q. Zhang and J. Guan, *Nano Res.*, 2022, **15**, 38–70.

7 Q. Zhang and J. Guan, *Adv. Funct. Mater.*, 2020, **30**, 1–53.

8 N. Cheng, L. Zhang, K. Doyle-Davis and X. Sun, *Electrochem. Energy Rev.*, 2019, **2**, 539–573.

9 M. D. Hossain, Z. Liu, M. Zhuang, X. Yan, G. L. Xu, C. A. Gadre, A. Tyagi, I. H. Abidi, C. J. Sun, H. Wong, A. Guda, Y. Hao, X. Pan, K. Amine and Z. Luo, *Adv. Energy Mater.*, 2019, **9**, 1–10.

10 D. N. Sredojević, M. R. Belić and Ž. Šljivančanin, *J. Phys. Chem. C*, 2020, **124**, 16860–

16867.

11 Y. Sun, A. Huang and Z. Wang, *RSC Adv.*, 2019, **9**, 26321–26326.

12 F. Ullah, K. Ayub and T. Mahmood, *Int. J. Hydrogen Energy*, 2021, **46**, 37814–37823.

13 S. Lu, H. L. Huynh, F. Lou, K. Guo and Z. Yu, *Nanoscale*, 2021, **13**, 12885–12895.

14 T. He, S. K. Matta, G. Will and A. Du, *Small Methods*, 2019, **3**, 1–7.

15 H. Chen, C. Zhu, C. Wen, M. Wang, M. Zhang, Y. Geng and Z. Su, *Appl. Surf. Sci.*, 2021, **549**, 149320.

16 X. Zhang, A. Chen, Z. Zhang, M. Jiao and Z. Zhou, *J. Mater. Chem. A*, 2018, **6**, 11446–11452.

17 B. Özdamar, G. Özbal, M. N. Çınar, K. Sevim, G. Kurt, B. Kaya and H. Sevinçli, *Phys. Rev. B*, 2018, **98**, 045431.

18 R. N. Somaiya, Y. A. Sonvane and S. K. Gupta, *Phys. Chem. Chem. Phys.*, 2020, **22**, 3990–3998.

19 H. Murari and S. Ghosh, *J. Phys. D. Appl. Phys.*, 2023, **56**, 295501.

20 R. N. Somaiya, D. Singh, Y. Sonvane, S. K. Gupta and R. Ahuja, *Catal. Sci. Technol.*, 2021, **11**, 4996–5013.

21 X. Liu, S. M. Cho, S. Lin, Z. Chen, W. Choi, Y.-M. Kim, E. Yun, E. H. Baek, D. H. Ryu and H. Lee, *Matter*, 2022, **5**, 2306–2318.

22 Y. Gao, H. Zhang, H. Pan, Q. Li and J. Zhao, *Nanotechnology*, 2021, **32**, 215402.

23 V. Mahamiya, A. Shukla, N. Garg and B. Chakraborty, *Int. J. Hydrogen Energy*, 2022, **47**, 7870–7883.

24 M. Singh, A. Shukla and B. Chakraborty, *Nanotechnology*, 2022, **33**, 405406.

25 S. Lakshmy, A. Kundu, N. Kalarikkal and B. Chakraborty, *J. Mater. Chem. B*, 2022, **10**, 5958–5967.

26 S. Lakshmy, A. Kundu, N. Kalarikkal and B. Chakraborty, *J. Phys. D. Appl. Phys.*, 2023, **56**, 055402.

27 M. Sajjad, K. Badawy, J. A. Larsson, R. Umer and N. Singh, *Carbon*, 2023, **214**, 118340.

28 P. Giannozzi et al., *J. Phys. Condens. Matter*, 2009, **21**, 395502.

29 J. P. Perdew, K. Burke and Y. Wang, *Phys. Rev. B*, 1996, **54**, 16533–16539.

30 S. Grimme, *J. Comput. Chem.*, 2006, **27**, 1787–1799.

31 H. J. Monkhorst and J. D. Pack, *Phys. Rev. B*, 1976, **13**, 5188–5192.

32 D. Singh, S. Chakraborty and R. Ahuja, *ACS Appl. Energy Mater.*, 2019, **2**, 8441–8448.

33 Q. Chang, X. Zhang and Z. Yang, *Appl. Surf. Sci.*, 2021, **565**, 150568.

34 X. Zhao, X. Yang, D. Singh, P. K. Panda, W. Luo, Y. Li and R. Ahuja, *J. Phys. Chem. C*, 2020, **124**, 7884–7892.

35 W. G. Lee, S. Chae, Y. K. Chung, W. S. Yoon, J. Y. Choi and J. Huh, *ACS Omega*, 2019, **4**, 18392–18397.

36 X.-B. Xiao, Q. Ye, Z.-F. Liu, Q.-P. Wu, Y. Li and G.-P. Ai, *Nanoscale Res. Lett.*, 2019, **14**, 322.

37 L. Xiong, B. Wang, H. Cai, T. Yang, L. Wang and S. Yang, *J. Mater. Chem. A*, 2020, **8**, 1184–1192.

38 Y. Zhou, G. Gao, J. Kang, W. Chu and L.-W. Wang, *Nanoscale*, 2019, **11**, 18169–18175.

39 A. Allangawi, M. A. Gilani, K. Ayub and T. Mahmood, *Int. J. Hydrogen Energy*, 2023, **48**, 16663-16677.

40 A. Allangawi, H. H. Shanaah, T. Mahmood and K. Ayub, *Mater. Sci. Semicond. Process.*, 2023, **162**, 107544.

41 D. Chen, Z. Chen, X. Zhang, Z. Lu, S. Xiao, B. Xiao and C. V. Singh, *J. Energy Chem.*, 2021, **52**, 155–162.